ACS Sustainable Chemistry & Engineering

Research Article

pubs.acs.org/journal/ascecg

# Plasmonic Bi/$ZnWO_4$ Microspheres with Improved Photocatalytic Activity on NO Removal under Visible Light

Yunxia Gao,[†] Yu Huang,[*,†,‡] Yan Li,[†] Qian Zhang,[†] Jun-ji Cao,[†,‡] Wingkei Ho,[†,§] and Shun Cheng Lee[∥]

[†]Key Laboratory of Aerosol Chemistry & Physics, Institute of Earth Environment and [‡]State Key Laboratory of Loess and Quaternary Geology (SKLLQG), Institute of Earth Environment, Chinese Academy of Sciences, Xi'an 710061, China

[§]Department of Science and Environmental Studies, The Hong Kong Institute of Education, Hong Kong, China

[∥]Department of Civil and Environmental Engineering, The Hong Kong Polytechnic University, Hung Hom, Hong Kong

Supporting Information

**ABSTRACT:** In this work, bismuth (Bi) nanoparticle anchored $ZnWO_4$ microspheres (Bi/$ZnWO_4$) were prepared and used as robust and efficient photocatalysts for NO removal at parts-per-billion level under visible light irradiation. The as-synthesized composite with a proper mass ratio of Bi (50%) displayed a higher reaction rate (0.067 $min^{-1}$) than its single counterparts $ZnWO_4$ (0.004 $min^{-1}$) and Bi (0.027 $min^{-1}$), respectively. Due to the surface plasmon resonance (SPR) effect of Bi nanoparticles, the Bi/$ZnWO_4$ composites showed broad light absorption in the visible spectrum. Moreover, the formation of the Bi/$ZnWO_4$ heterointerface promoted the separation of photoexcited electron−hole pairs, which is demonstrated by the increased photocurrent density in comparison to the pristine materials. The above characteristics endowed the Bi/$ZnWO_4$ composites with superior photocatalytic activity for NO removal. The radical scavanger tests revealed that the superoxide radical was the main active species to initiate NO oxidation, while the hydroxyl radical was not involved in the process. This study shows practical value in air pollutant abatement, because it provides an economical and feasible route to fabricate SPR-enhanced composite photocatalysts using earth abundant Bi material instead of noble metals.

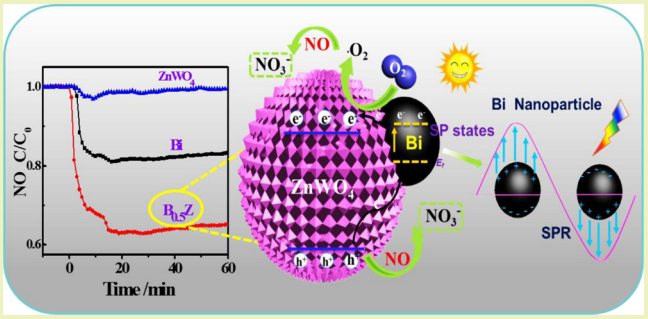


**KEYWORDS:** *Bi/$ZnWO_4$ nanocomposites, Photocatalysis, Surface plasmon resonance effect (SPR), Intermediates, NO removal*

## INTRODUCTION

Nitrogen oxides ($NO_x$, the sum of NO and $NO_2$), exclusively originated from fossil fuels combustion and vehicular exhaust, are important precursors for atmospheric secondary organic aerosols (SOAs) formation,[1] which can impose an adverse effect on air quality and human health.[2] Therefore, efficient techniques are stringently needed to eliminate the emitted $NO_x$ in the atmosphere. Among the various de$NO_x$ strategies, semiconductor photocatalysis is a promising green technique which can be operated at ambient pressure and temperature.[3−5] However, the development of photocatalytic nanomaterials with visible-light-harvesting capability and high quantum yield is still challenging.[6,7]

$ZnWO_4$ with a wolframite structure has been widely studied as a promising photocatalyst for water splitting and mineralization of organic pollutants because of its intrinsic structural property.[8−10] The $ZnWO_4$ photocatalyst with different microstructures and tunable properties has been reported in order to enhance its photocatalytic activity.[9,11] Most recently, our research group adopted the ultrasonic spray pyrolysis (USP) method to fabricate porous $ZnWO_4$ microspheres, and the resulting microspheres exhibited superior photocatalytic activity for $NO_x$ abatement under solar light irradiation than that of commercial P25, which can be ascribed to the facilitated separation/diffusion of the photogenerated charge carriers and the diffusion of intermediates and final products due to the presence of the porous structure.[12] Nevertheless, its wide bandgap resulted in the poor visible light response and hindered the practical application in air pollution control. To overcome these drawbacks, various strategies such as element doping,[13,14] morphology tuning,[8] and heterostructure construction[15,16] were developed. For example, $ZnWO_4$ was modified by fluorine and cadmium ions doping to improve the photocatalytic activity, respectively.[11,17] $Bi_2O_2CO_3$/$ZnWO_4$ composite photocatalysts were constructed by the hydrothermal method successfully, and the catalysts exhibit higher photocatalytic activity than a pure single-component photocatalyst.[18] Although these methods can partly enhance the efficiency of $ZnWO_4$, the sufficient utilization of solar light remains limited.

The deposition of noble metal nanoparticles (such as Au, Ag, and Pt) on semiconductors provides an alternative method to

Received: August 4, 2016
Revised: September 30, 2016
Published: October 19, 2016

  

DOI: 10.1021/acssuschemeng.6b01852
ACS Sustainable Chem. Eng. XXXX, XXX, XXX−XXX

improve the light absorption range and ability of wide-bandgap semiconductors because of the formation of the Schottky barrier at the interface.[19] After noble metal coupling, the electrons on the nanoparticles undergo a collective oscillation induced by the impinging light when their oscillating frequencies are matched, giving rise to the so-called surface plasmon resonance (SPR).[19] For example, the deposition of Ag nanoparticles on $SrTiO_3$ incurs a broad plasmonic resonance absorption in the visible light range, resulting in enhanced visible light driven activity on NO removal in comparison with pristine $SrTiO_3$.[20] The surface plasmon resonance effect can be tuned by controlling the size, morphology, and surrounding environment. Considering the high cost of these precious metals, semimetal bismuth (Bi), of high earth abundance, has attracted a great deal of attention in view of its unique properties, including small band overlap energy, low electron effective mass, and low charge carrier density.[21−23]

Previous studies showed that Bi nanoparticles exhibit surface plasmon resonance (SPR), which is sensitive to the size, shape, and organization of the nanoparticles.[24] Dong and co-workers employed the chemical solution method to prepare Bi nanoparticles with a size of around 100−200 nm, which can serve as a direct plasmonic photocatalyst.[25] Several Bi deposited composite photocatalysts, such as Bi/BiOCl,[26,27] Bi/BiOI,[28] $Bi/(BiO)_2CO_3$,[29,30] $Bi/Bi_2MoO_6$,[31] $Bi/g\text{-}C_3N_4$,[32] and $Bi/Bi_2O_3$,[33] have been reported. All these semiconductors coupled with the Bi element exhibited a highly promoted photocatalytic performance. However, to the best of our knowledge, the synthesis, photocatalysis mechanism, and application of $Bi/ZnWO_4$ have never been reported.

In this study, we employed a facile solvothermal method to couple Bi nanoparticles on the as-prepared $ZnWO_4$ hollow microspheres. The photocatalytic performance of the as-prepared composites with different mass ratios was also evaluated by NO in air degradation under visible light irradiation. The photoinduced active species and intermediate products were also identified. Furthermore, the degradation mechanism was proposed for NO degradation over $Bi/ZnWO_4$ composites.

## EXPERIMENTAL SECTION

**Preparation of Pristine $ZnWO_4$ Hollow Microspheres and $Bi/ZnWO_4$ Composites.** All chemicals used in our experiment were of analytical grade and were used without further purification. The $ZnWO_4$ microspheres were fabricated through ultrasonic spray pyrolysis as reported in our previous work.[12] In brief, $Zn(NO_3)_2 \cdot 6H_2O$ (10 mmol) and $H_2WO_4$ (10 mmol) were dissolved in deionized water (50 mL) and concentrated ammonia (10 mL), respectively. The tungstic acid/ammonia solution was added into the $Zn(NO_3)_2$ aqueous solution and stirred for about half an hour and transferred into an ultrasonic nebulizer (YUYUE 402AI, Shanghai, China) operated at a fixed frequency of 1.7 MHz ± 10%. The atomized droplets were carried by air flow into a tube furnace (OTF-1200X, Hefei, China) and subjected to thermodecomposition at a constant temperature of 700 °C. The as-obtained white precipitates were collected in an absorption bottle.

$Bi/ZnWO_4$ composites were synthesized via a typical solvothermal method. First, 1 mmol of Bi $(NO_3)_3 \cdot 5H_2O$ and 1 mmol of glucose were mixed in 30 mL of ethylene glycol under continuous stirring. After the mixture was dissolved completely, a certain amount of the as-prepared $ZnWO_4$ powders was added and ultrasonically dispersed. The final precursor suspensions were transferred into a 50 mL Teflon-lined autoclave with a stainless steel vessel and heated at 160 °C for 24 h. Finally, the precipitates were collected, washed with ethanol and deionized water several times after cooling down to room temperature, and dried at 70 °C for 4 h. For convenience and clarity, the synthesized $Bi/ZnWO_4$ composites were denoted as $B_xZ$, where $x$ represents the mass ratio of Bi to (Bi + $ZnWO_4$). The resulting composites with $x$ values of 0.3, 0.4, 0.5, and 0.6 were labeled as $B_{0.3}Z$, $B_{0.4}Z$, $B_{0.5}Z$, and $B_{0.6}Z$, respectively. For comparison, Bi nanoparticles were prepared under other identical conditions without the addition of $ZnWO_4$.

**Characterization.** The crystalline structure of the as-obtained samples was determined by using an X-ray powder diffractometer (XRD; PANanalytical, X'pert, The Netherlands) with a Cu K$\alpha$ radiation source ($\lambda$ = 1.5406 Å) at a scan step size of 0.017° in the 2$\theta$ range of 10°−80°. The morphological characteristics and microstructures of the samples were examined by using a field-emission scanning electron microscope (FE-SEM; equipped with energy dispersive X-ray spectrometry (EDXS), JEOL Model JSM-6700F, Japan) and a transmission electron microscope (TEM; JEM-2100HR). The Brunauer−Emmett−Teller (BET) surface area and pore structure of samples were obtained from the adsorption branch of the isotherms and Barrett−Joyner−Halenda formula at 77 K by using a Gemini VII 2390 analyzer (Micromeritics Instrument Corp., Norcross, GA, USA). The surface characteristics of the samples were investigated through X-ray photoelectron spectroscopy (XPS; Escalab 250Xi, the United States) equipped with a monochromatic Al K$\alpha$ source and a charge neutralizer. The optical properties of the catalysts at 200−800 nm were obtained using a Varian Cary 100 Scan UV−visible system (UV−vis; Agilent corp., the United States) with a Labsphere diffuse reflectance accessory. $Ba_2SO_4$ was used as a reflectance standard. Fourier transform infrared (FT-IR) spectra were recorded on a FTIR absorption spectrometer (VERTEX 70, BRUKER), with KBr as the diluent. Photoluminescence (PL; F-7000, Hitachi, Japan) was also obtained to investigate the optical properties of the resulting samples.

**Photocatalytic Activity Assessment.** The photocatalytic activities of samples were investigated by degrading NO at ppb levels in a continuous flow reactor at ambient temperature under visible light irradiation. The reaction chamber was composed of a rectangular stainless steel vessel (30 cm L × 15 cm W × 10 cm H) and covered with a quartz window. Visible light was supplied by a 300 W xenon lamp (Perfect Light MICROSOLAR 300, Beijing, China) with a UV cutoff filter ($\lambda$ > 420 nm), which vertically passed through the quartz window. For each photocatalytic activity experiment, one sample dish (diameter = 12 cm) containing the photocatalyst powders was placed at the center of the reactor. The photocatalyst samples were prepared by coating an aqueous suspension of the products onto a glass dish. The weight of the photocatalysts used for each experiment was maintained at 100 mg. The dishes containing the photocatalyst were pretreated at 70 °C for several hours until water in the suspension was completely removed. Then, the pretreated dishes were cooled to room temperature prior to the photocatalysis test.

NO gas with an initial concentration of 50 ppm was obtained from a compressed gas cylinder. The initial concentration of NO used in the photocatalysis test was diluted to 400 ppb with an air stream supplied by a zero air generator (Model 1001, Sabio Instruments LLC, Georgetown, TX, USA). The desired humidity level of the NO flow was controlled at 70% by passing the zero air streams through a humidification chamber. The gas streams were premixed completely by a gas blender, and the flow rate was controlled at 3 L/min by using a mass flow controller. After the catalyst achieved adsorption/desorption equilibrium, the xenon lamp was switched on. The NO and $NO_2$ concentrations were continuously measured with a chemiluminescence $NO_x$ analyzer (Model 42c, Thermo Environmental Instruments Inc., Franklin, MA, USA) during photocatalytic degradation at a sampling rate of 0.6 L/min. The reaction of NO with air was negligible in the control experiment performed with or without light in the absence of the photocatalyst. The removal ratio of NO at any given time was noted as $C/C_0$, where $C$ is the NO concentration of the outlet at any given time, and $C_0$ is the initial concentration of NO, ppb. The yields of $NO_2$ over different photocatalysts are calculated by the following equation[34]


DOI: 10.1021/acssuschemeng.6b01852
ACS Sustainable Chem. Eng. XXXX, XXX, XXX−XXX

$$NO_2 \text{ yields} = \frac{C_{NO_2}}{C_0 - C}$$

where $C_{NO_2}$ is the production of $NO_2$, ppb.

**Trapping Experiments for the Identification of Visible-Light-Induced Active Species.** Potassium iodide (KI) and *tert*-butyl alcohol (TBA) are effective hole and hydroxyl radical (·OH) scavengers, respectively. Potassium dichromate ($K_2Cr_2O_7$) was utilized as photoinduced electron scavenger. Photocatalysts (100 mg) containing different trapping agents were prepared by adding 20 mL of deionized water and were ultrasonicated for 30 min; the additive amount of all scavengers was 1%. The dispersed suspensions were coated onto glass sample dishes dried at 60 °C until water was removed completely. The dried dishes were used in NO removal experiments.

**Photoelectrochemical Measurements.** The photoelectrochemical properties of the as-prepared samples were evaluated using an electrochemical workstation (PARSTAT-4000, Advanced Measurements Technology, Inc., USA) in a conventional three-electrode cell, in which a platinum plate and an Ag/AgCl electrode were used as a counter electrode and a reference electrode, respectively. Afterward, 25 mg of Bi/$ZnWO_4$ composites was dispersed into 5 mL of 1 wt % Nafion ethanol solution to obtain a homogeneous suspension through bath sonication and thus fabricate a working electrode. The films were subsequently modified on a 10 mm × 10 mm fluorine-doped tin oxide conducting glass by using a dip coater (ZR-4200, Qingdao, China). The modified films were then allowed to dry under ambient conditions. A 300 W Xe arc lamp (Perfect Light MICROSOLAR 300, Beijing, China) with a UV cutoff filter ($\lambda > 420$ nm) was used as a light source. Current−time curves were determined at 0.2 V versus Ag/AgCl in $Na_2SO_3$ (0.1 mol/L) at ambient temperature, and the flat band potential is measured through Mott−Schottky plot at a frequency of 1 kHz in 0.1 mol $L^{-1}$ $Na_2SO_4$.

## RESULTS AND DISCUSSION

**Phase Structure, Morphologies, and Surface Chemical Composition.** Figure 1 shows the XRD patterns of Bi nanoparticles, pristine $ZnWO_4$ microspheres, and the as-prepared Bi/$ZnWO_4$ composites. The sharp diffraction peaks of Bi can be well indexed as rhombohedral Bi (JCPDS No. 85-1329, space group of $R\bar{3}m$). The XRD pattern of $ZnWO_4$ shows typical diffraction peaks located at 18.9°, 23.7°, 24.5°, 30.5°, 36.3°, 41.2°, 53.7°, 61.9°, and 64.8° of the monoclinic wolframite structure (JCPDS No. 88-0251, space group of $P2/c$). The diffraction peaks of Bi and $ZnWO_4$ are both present in the XRD patterns of the as-prepared Bi/$ZnWO_4$ composites.

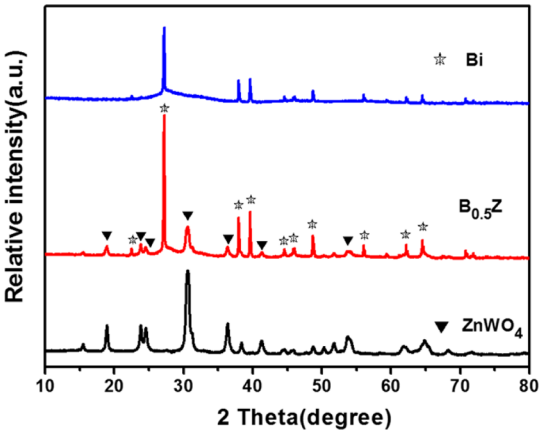


**Figure 1.** Powder XRD patterns of the as-prepared pristine $ZnWO_4$ microspheres, Bi, and $B_{0.5}Z$ composites.

Moreover, the intensity of the diffraction peaks of Bi and $ZnWO_4$ in Bi/$ZnWO_4$ composites presents obvious variations compared with the corresponding pristine component, indicating the interactions between the two components during the synthesis processes.

The morphologies of the as-prepared samples were examined by using SEM and TEM analysis. As displayed in Figure 2a, the pristine $ZnWO_4$ samples are composed of hierarchical porous microspheres with a diameter ranging from 0.1 to 2 $\mu$m, which is consistent with our previous results.[12] Bi nanoparticles with a size of approximately 100 nm tightly anchor on the surface of $ZnWO_4$ to be assembled into Bi/$ZnWO_4$ composites as shown in Figure 2b. To identify the specific composition of the $B_{0.5}Z$ composites, EDX analysis (Figure 2c) was performed, and it was shown that the atomic ratio of Zn:W:O:I is 1.0:1.1:6.3:0.3. The molar ratio of Zn to O in $B_{0.5}Z$ is about 1:6.3, which is higher than that in $ZnWO_4$ (1:4). This suggests that the surface of the as-prepared composites is slightly rich in oxygen, which can be ascribed to the presence of the $Bi_2O_3$ amorphous layer on Bi nanoparticles oxidized by oxygen in air. The SEM image of the composite (Figure 2d) and the elemental mapping images of the same low region indicate that Zn, O, W, and Bi elements are homogeneously distributed on the obtained composites (Figure 2e-h).

Figure 3a and b shows the TEM images of the $ZnWO_4$ microspheres and $B_{0.5}Z$ composites. As displayed, the $ZnWO_4$ microspheres exhibit an obvious porous structure (Figure 3a), while the composites consist of solid spheres (Figure 3b) which can be ascribed to the filling of the pore structures by Bi nanoparticles during the synthesis processes. Table 1 lists the BET surface area, the total pore volume, and average pore size value of as-obtained $ZnWO_4$, $B_{0.5}Z$ composite, and Bi. As anticipated, the corresponding pore size of the Bi/$ZnWO_4$ composite is inferior to pristine $ZnWO_4$ after introducing Bi, while the specific BET surface area is higher than that of $ZnWO_4$. This might be attributed to the agglomeration of Bi/$ZnWO_4$ composites. The corresponding HR-TEM images were shown in Figure 3c and d. Distinct lattice fringe in pristine $ZnWO_4$ samples was observed ($d$ = 0.293 nm), which corresponds to the (111) lattice plane. For $B_{0.5}Z$ composites, the lattice spacing of Bi with the (012) lattice plane of approximately 0.326 nm can also be resolved. Furthermore, it can be clearly observed that the interface between $ZnWO_4$ and Bi nanoparticles was formed in Bi/$ZnWO_4$ composites, which is beneficial for the transmission of photogenerated carriers between semimetal Bi and $ZnWO_4$ microspheres.[18,27,29]

The surface chemical composition and valence states of elements in the $B_{0.5}Z$ composites were further analyzed by XPS (Figure 4). The survey spectrum in Figure 4a implies the presence of Zn, W, Bi, and O in the as-prepared composite sample without other elemental signals being detected. High-resolution XPS (Figure 4b) reveals that the 4$f$ peaks of Bi fit into a doublet corresponding to Bi $4f_{5/2}$ (164.3 eV) and Bi $4f_{7/2}$ (159.0 eV), which are characteristics of $Bi^{3+}$ in $Bi_2O_3$.[35,36] Therefore, the surface layer of semimetal Bi mainly exists in the form of bismuth oxide. Furthermore, distinct binding energy drifts in the $B_{0.5}Z$ composites were observed, which could be attributed to the formation of a contact interface between metallic Bi and $ZnWO_4$ in the Bi/$ZnWO_4$ composite instead of a simple physical mixture, and the same phenomenon is observed in the spectra of Zn 2$p$ and W 4$f$ (Supporting Information, Figure S1a and b). To verify the existence of $Bi^0$, we performed a sputtering experiment (Figure 4c). Comparing


DOI: 10.1021/acssuschemeng.6b01852
ACS Sustainable Chem. Eng. XXXX, XXX, XXX−XXX

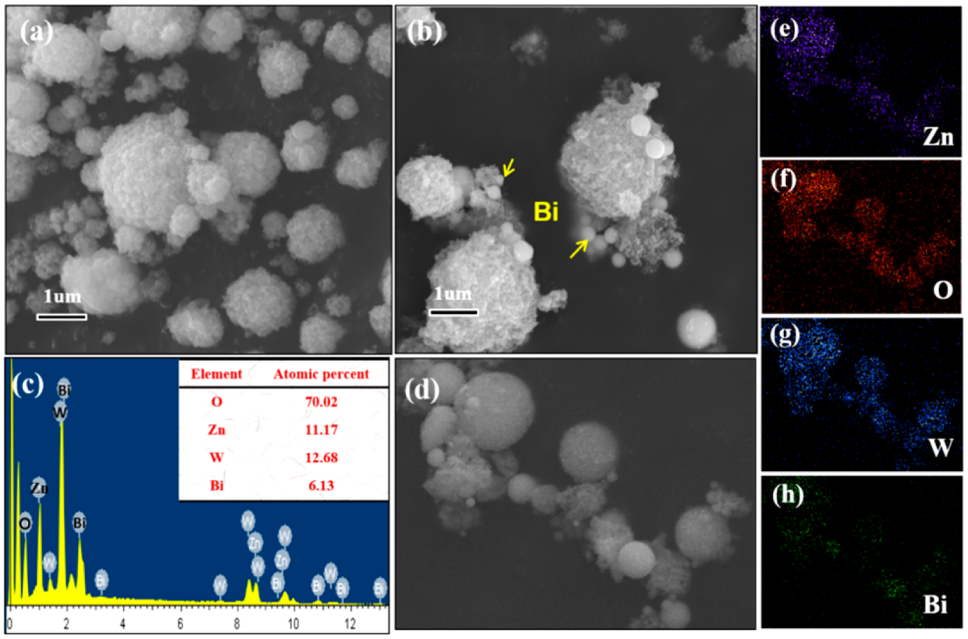


**Figure 2.** SEM images of pristine $ZnWO_4$ microspheres (a) and $B_{0.5}Z$ nanocomposites (b); FE-SEM-EDX images of the $B_{0.5}Z$ composites (c); and SEM image of composites (d) and elemental distribution maps of the corresponding low region indicating the spatial distribution of Zn (e), O (f), W (g), and Bi (h).

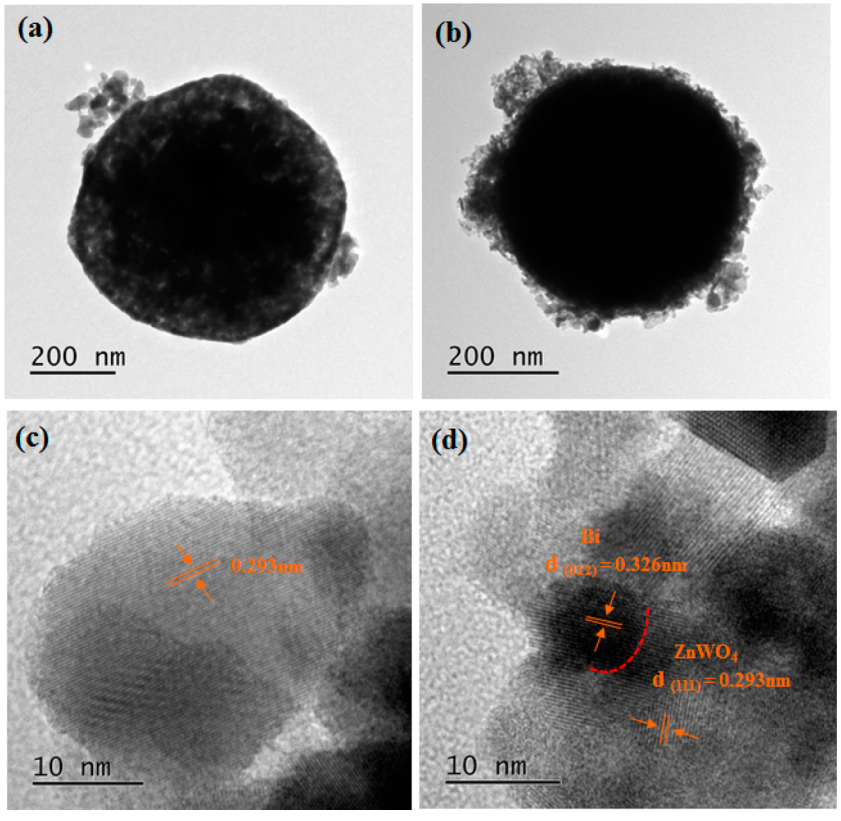


**Figure 3.** Low-magnification TEM images of pristine $ZnWO_4$ (a) and $B_{0.5}Z$ nanocomposites (b) and HRTEM images of $ZnWO_4$ (c) and $B_{0.5}Z$ composites (d).

the Bi 4*f* spectra of the $B_{0.5}Z$ composite before and after ion etching for 180 s, two new diffraction peaks were found at approximately 156.9 and 162.2 eV, which are typically attributed to the Bi−Bi bond of Bi.[37,38] Three main peaks can also be separated in the O 1*s* spectrum of the $B_{0.5}Z$ composites (Figure 4d). The peaks with binding energies of 529.5, 530.3, and 531.2 eV are also identified, which can be respectively ascribed to the Bi−O bonds in $Bi_2O_3$, the Zn−O bonds in $ZnWO_4$, and the adsorbed oxygen on the sample surface.



DOI: 10.1021/acssuschemeng.6b01852
ACS Sustainable Chem. Eng. XXXX, XXX, XXX−XXX

**Table 1. Brunauer–Emmett–Teller (BET) Surface Area, Pore Volume, Pore Size, and Reaction Rate Constant for $ZnWO_4$, $B_{0.5}Z$, and Bi**

| samples | $S_{BET}$ ($m^2/g$) | $V_p$ ($cm^3/g$) | pore size (nm) | reaction rate constant $k$ ($min^{-1}$) |
|---|---|---|---|---|
| $ZnWO_4$ | 13.7 | 0.12 | 33.1 | 0.004 |
| $B_{0.5}Z$ | 29.6 | 0.11 | 12.8 | 0.067 |
| Bi | 15.9 | 0.16 | 34.5 | 0.027 |

**Optical Property.** The UV–vis DRS of the pristine $ZnWO_4$ microspheres and Bi/$ZnWO_4$ composites are shown in Figure 5. It is clearly observed that pristine $ZnWO_4$ harvested the majority of light below 400 nm, while the light absorption ability of the Bi/$ZnWO_4$ composite is significantly enhanced ranging from the UV light to near-infrared light after Bi deposition (200–800 nm). This phenomenon could be assigned to a charge-transfer transition between the Bi nanoparticles and the $ZnWO_4$ microspheres, which is also in agreement with the color variation of the composite. A distinct surface plasmon resonance (SPR) peak centered at 460 nm can be observed for pure Bi.[24,39,40] Furthermore, the absorption edge and the characteristic SPR absorption of the Bi/$ZnWO_4$ composite shift to a higher-wavelength range (from 460 to 520 nm) possibly caused by the different sizes of Bi nanoparticles.[24] This strengthened light absorption is crucial for photoexciting more electrons and holes to enhance the photocatalysis efficiency of the Bi/$ZnWO_4$ composites. Therefore, the introduction of metallic Bi enhances visible light absorption because of its SPR effect.

**Photocatalytic Activity and Production of Intermediates.** The photocatalytic performances of pristine $ZnWO_4$, Bi nanoparticles, and the as-prepared Bi/$ZnWO_4$ with different mass ratios were evaluated on the degradation of NO in air under visible light irradiation ($\lambda$ > 420 nm) in a continuous reactor. The NO removal rates against irradiation time over different photocatalysts are plotted in Figure 6a, where $C_0$ is the initial concentration of NO, and $C$ is the concentration of NO after photocatalytic degradation for time $t$. As observed, pristine $ZnWO_4$ exhibited a negligible visible light activity for NO removal, which can be ascribed to its large band gap energy. However, after the deposition of Bi nanoparticles on $ZnWO_4$,

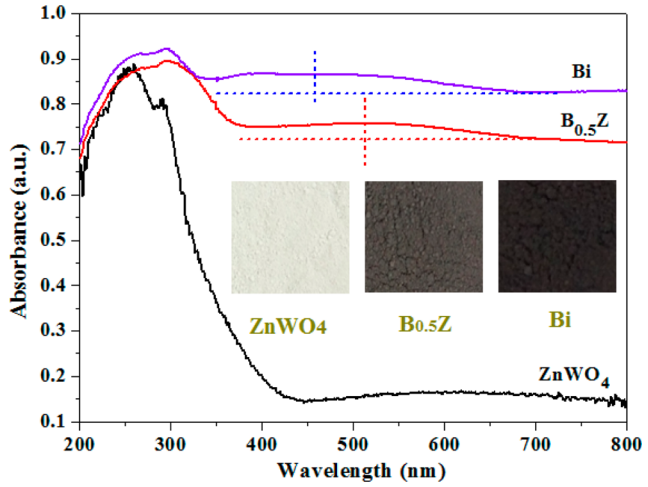


**Figure 5.** UV–vis diffuse reflectance spectra (DRS) of pristine $ZnWO_4$ microspheres, Bi, and $B_{0.5}Z$ nanocomposites (The inset shows the photographs of corresponding samples.).

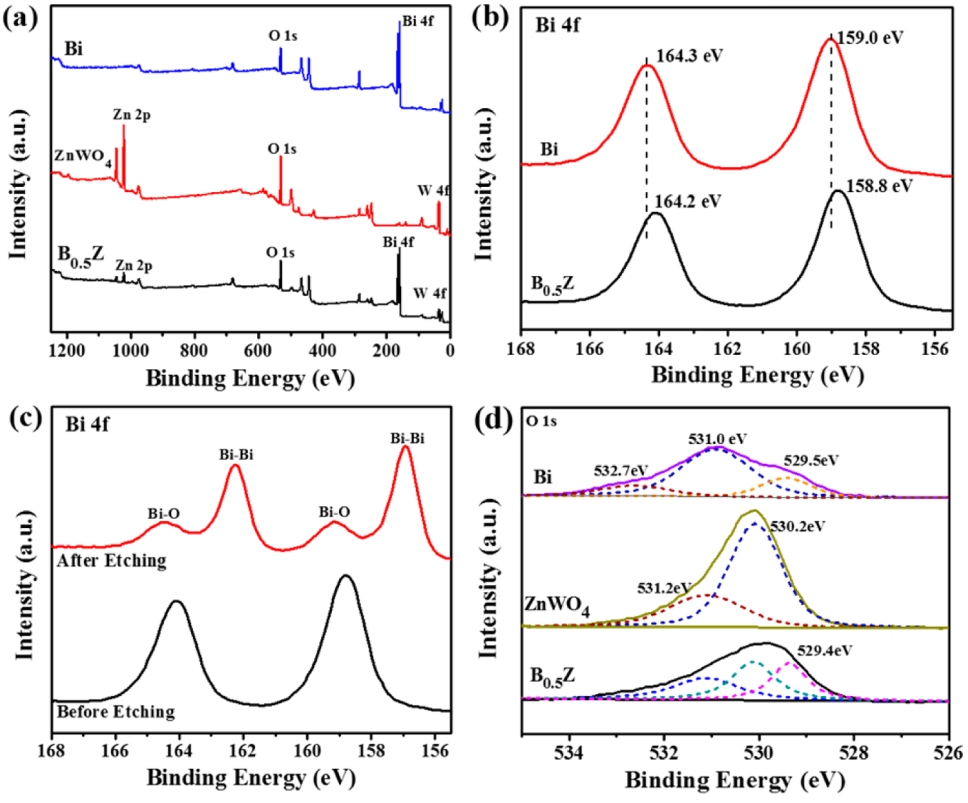


**Figure 4.** XPS spectra of as-prepared samples: (a) survey spectrum; (b) Bi 4*f* spectrum; (c) Bi 4*f* spectrum of $B_{0.5}Z$ composites before and after ion etching; and (d) O 1*s* spectrum.


DOI: 10.1021/acssuschemeng.6b01852
ACS Sustainable Chem. Eng. XXXX, XXX, XXX–XXX

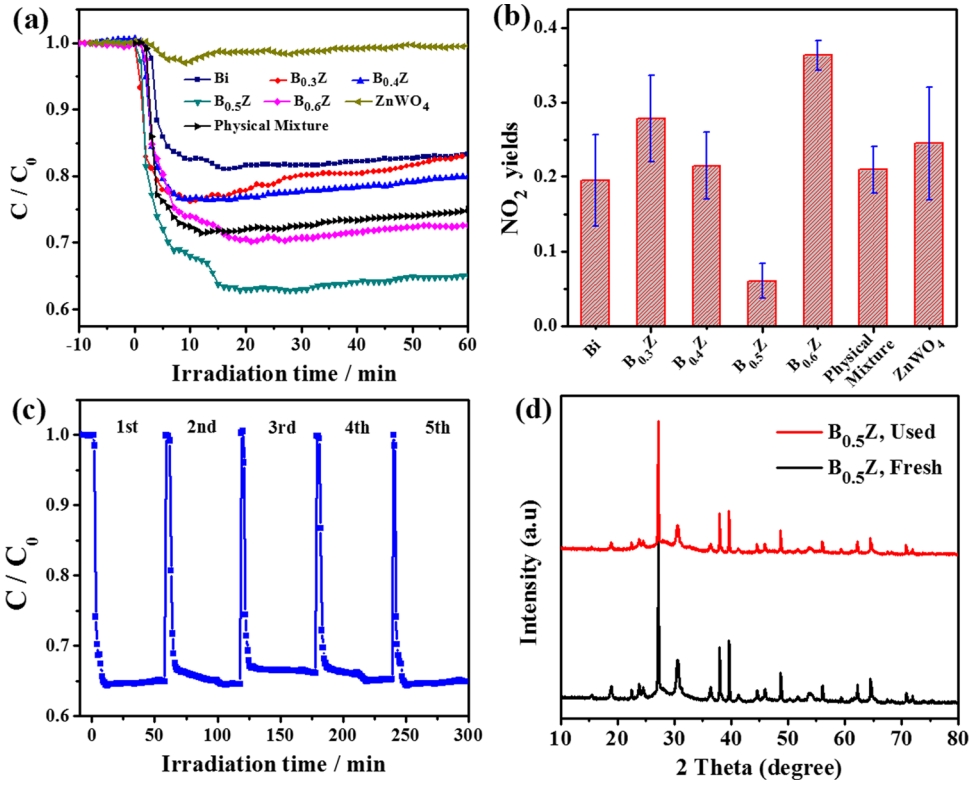


**Figure 6.** (a) NO removal efficiency ($C/C_0$) against irradiation time over $ZnWO_4$, Bi, and Bi/$ZnWO_4$ composites with different mass ratios and the physical mixture composed of 50% $ZnWO_4$ and 50% Bi under visible light ($\lambda$ > 420 nm); (b) the corresponding $NO_2$ yields over as-prepared samples; (c) photochemical stability of the $B_{0.5}Z$ nanocomposites; and (d) XRD spectra of $B_{0.5}Z$ composites before and after photocatalytic activity tests.

the Bi/$ZnWO_4$ composites present significantly enhanced photocatalytic activities. For comparison, the mechanical mixture with equivalent element Bi (reference $B_{0.5}Z$) was also prepared under identical conditions. As shown in Figure 6a, with the increase of the Bi loading ratio from 0.3 to 0.6, the photocatalytic activities increase initially and then decreased with the mass ratio over 0.5. Among the four Bi/$ZnWO_4$ composite samples, $B_{0.5}Z$ showed the best NO removal performances, with 37% of NO eliminated, which is more than two times higher than that of pure Bi nanoparticles (17%). Furthermore, the photocatalytic activity of $B_{0.5}Z$ is much higher than that of the physical mixture sample, indicating the existence of a synergistic effect of the $B_{0.5}Z$ composite. Notably, the initial photocatalytic degradation of NO was recognized to follow mass transfer controlled first-order kinetics comparatively as a result of low-concentration target pollutants, as evidenced by the linear plot of $\ln(C/C_0)$ versus photocatalytic reaction time $t$. As shown in Figure S2, the rate constant is 0.067 $min^{-1}$ for the $B_{0.5}Z$ composite, which is 2.5, 1.5, 1.5, 1.6, 1.4, and 16.7 times higher than those of the Bi (0.027 $min^{-1}$), $B_{0.3}Z$ (0.044 $min^{-1}$), $B_{0.4}Z$ (0.044 $min^{-1}$), $B_{0.6}Z$ (0.041 $min^{-1}$), physical mixture (0.048 $min^{-1}$), and pristine $ZnWO_4$ (0.004 $min^{-1}$) samples, respectively. Moreover, toxic intermediate $NO_2$ during the photocatalytic processes was also identified. As shown in Figure 6b, the $B_{0.5}Z$ composite presented the lowest $NO_2$ yields (about 6%), suggesting that the composites are more advantageous for the removal of $NO_x$ under realistic conditions.

The multiple runs of the photocatalytic activity test showed that the activity of $B_{0.5}Z$ composites is largely maintained (Figure 6c). Additionally, the catalyst is structurally stable, as indicated by the nearly unchanged XRD spectra (Figure 6d) and SEM images (Figure S3) of the samples before and after the stability test.

**Photoelectrochemical Analysis, Trapping Experiments, and Degradation Mechanism of NO.** Essentially speaking, the charge separation and transfer is a key process for the activity improvement of composite photocatalysts. To validate the effect of the metal−semiconductor interface, transient photocurrent responses of $ZnWO_4$, Bi, and $B_{0.5}Z$ electrodes in on−off cycles under visible light irradiation were also performed. As shown in Figure 7, when the light source was turned on, the photocurrent was rapidly increased and kept highly stable, whereas the value decreased immediately after the lamp was turned off, suggesting that the as-prepared electrodes possess fast photoelectric response ability. The highest photocurrent density at potential of 0.2 V (about 1.1 uA/$cm^2$) from $B_{0.5}Z$ composites is 3.7 and 2.2 times of those induced by pristine $ZnWO_4$ (0.3 uA/$cm^2$) and Bi (0.5 uA/$cm^2$), respectively. This distinctly enhanced photocurrent indicates that the formation of the Bi/$ZnWO_4$ heterointerface can efficiently accelerate the separation of photoexcited electron−hole pairs. The same tendency was also obtained from the photoluminescence (PL) spectra, in which the composite samples exhibit a lower PL signal than the pristine $ZnWO_4$ microspheres do, suggesting a considerably low recombination efficiency of electron−hole pairs (see Supporting Information, Figure S4).

Based on the photoelectrochemical analytical results, the band configuration of the Bi-$ZnWO_4$ composite is tentatively proposed to further illustrate the charge separation mechanism across the metal−semiconductor interface. Herein, the flat band


DOI: 10.1021/acssuschemeng.6b01852
ACS Sustainable Chem. Eng. XXXX, XXX, XXX−XXX

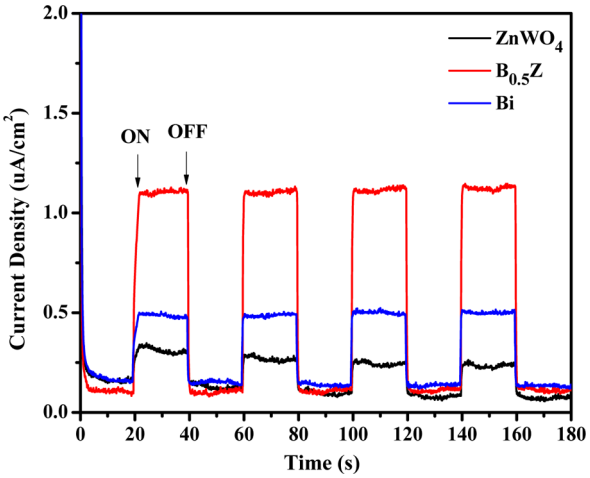


**Figure 7.** Transient photocurrent density-time curves of as-obtained sample electrodes at the potential of 0.2 V versus Ag/AgCl in $Na_2SO_3$ (0.1 mol/L) under visible light irradiation ($\lambda$ > 420 nm).

potential and Eg of $ZnWO_4$ microspheres were obtained using Mott−Schottky plots and the UV−visible diffuse reflectance absorption, as shown in Figure S5. The calculated bandgap energy of $ZnWO_4$ was estimated to be 3.71 eV. As the typical n-type semiconductor, the flat band potential is close to the conduction band position of $ZnWO_4$, which is marked as −0.53 V vs NHE (at pH 7), and thus the valence band is 3.18 V vs NHE (at pH 7). Apparently, the original $ZnWO_4$ cannot be excited under visible light due to its broad band gap energy. When semimetal Bi and semiconductor are in direct contact, the visible light absorption is strongly enhanced which is similar to the dye-sensitized process, as demonstrated by UV−vis results. Regarding this phenomenon several reporters have ascribed it to the SPR effect,[29,32] which has been studied intensely in recent years. The surface plasmon is produced when incoming photons interacting with surface electrons on metals at certain frequency result in resonance and strong optical absorption.[41] Thus, this effect has significant implications on photocatalytic reactions. Due to the proper dielectric functions of noble metals Au and Ag, they can support excellent optical absorption in visible light to infrared range, while semimetal Bi was found to exhibit strong resonance between near-ultraviolet and visible region.[24] As in our case, when plasmonic metal (Bi) and $ZnWO_4$ are in direct contact, with the formation of heterointerface semimetal Bi with SPR function digests the photons to produce the excited electrons (SP state higher than the CB of $ZnWO_4$) under visible light irradiation and donates free electrons to the CB of $ZnWO_4$,[20] as shown in Figure 8, thereby decreasing the recombination rates of electron−hole pairs. Meanwhile, when the electrons from Bi are released, the potentials drop rapidly, and it has the potential to capture electrons directly from the VB of $ZnWO_4$ and ensure that its original state is restored. During electrons and holes transfer at the interface, the recombination of electron−hole pairs is decreased, and the lifespan of the charge carriers from Bi is extended, consequently enhancing the visible photocatalytic activity.

To probe the photocatalytic degradation mechanism of NO in air under visible light irradiation, we performed trapping experiments to identify the involved active species in NO degradation. Figure 9 illustrates that TBA, as an effective ·OH scavenger, can hardly reduce the photocatalytic removal rate of

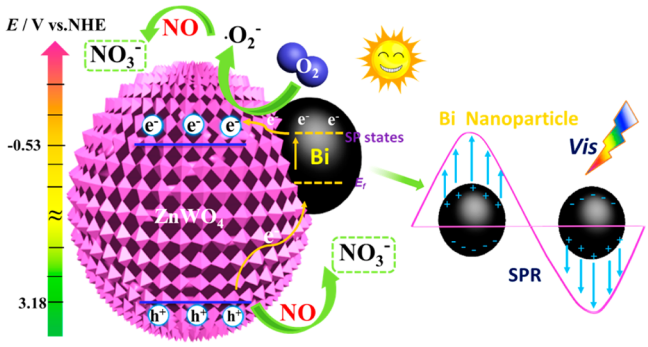


**Figure 8.** Mechanism of the NO removal and the visible light-driven ($\lambda$ > 420 nm) charges transfer between the pristine $ZnWO_4$ microspheres and semimetal Bi with SPR effect.

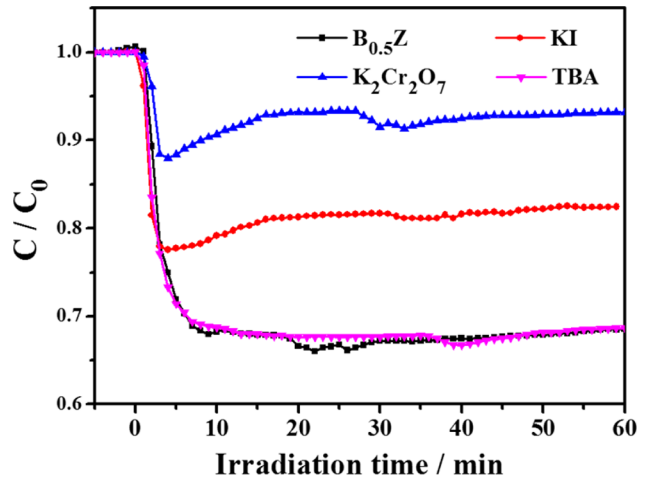


**Figure 9.** Photocatalytic degradation of NO with the addition of different active species trapped for $B_{0.5}Z$ samples.

NO. Thus, ·OH is not the main active species in the $B_{0.5}Z$ nanocomposite. However, the addition of $K_2Cr_2O_7$ and KI, especially the addition of an electronic capture agent and the holes scavenger, can largely decrease the rate of NO removal from the $B_{0.5}Z$ composites. This result indicated that the photoinduced electrons and holes are mainly involved active species for NO photocatalytic degradation. As shown in Figure 8, after the photoinduced charge carriers are separated, the aggregated electrons on the CB of $ZnWO_4$ are then captured by the surface-adsorbed $O_2$ to produce $\cdot O_2^-$, and final $\cdot O_2^-$ can efficiently destroy air pollutants. The excited electrons from the Bi surface should be with equal force. In addition, the photoinduced holes play an important role in NO removal. Presumably, the photogenerated holes in Bi nanospheres capture the electrons from the nearby VB of $ZnWO_4$ rather than directly acting on target pollutants.[29] Thus, the holes remaining on the VB of $ZnWO_4$ directly oxidize the gaseous pollutants, and ·OH does not contribute to NO removal. We speculate that the introduction of semimetal Bi can suppress the generation of ·OH on the $ZnWO_4$ samples, and the similar phenomenon was described in a previous study.[32] Qu et al.[42] also demonstrated that ·OH was not the main active oxidative species in $Bi@Bi_2O_3$@carboxylate-rich carbon spheres. The holes left in VB of $ZnWO_4$ possibly can further react with surface hydroxyl group/water to produce ·OH. Unfortunately, the output of ·OH is possibly much lower than that of $\cdot O_2^-$. $\cdot O_2^-$ is the main active species. NO degradation on the $ZnWO_4$


DOI: 10.1021/acssuschemeng.6b01852
ACS Sustainable Chem. Eng. XXXX, XXX, XXX−XXX

and Bi surface also occurs rapidly; as such, the function of ·OH becomes negligible. These results further confirmed that the inexpensive semimetal Bi nanoparticles can improve the visible light photocatalytic performance of the $ZnWO_4$ microspheres because of the SPR effect.

It has been reported that nitrate ($NO_3^-$) during the photocatalytic processes is the major NO degradation product and is accompanied by a small amount of intermediates (nitrite ions, $NO_2^-$).[43] In our case, the relative accumulated amount on the photocatalytic surface was determined after activity test, and the results were shown in Table S1 (Supporting Information). It was found that the amount of $NO_3^-$ on $B_{0.5}Z$ nanocomposites was the highest and up to 1276.2059 μg/g, followed by $ZnWO_4$ (106.7741 μg/g) and Bi (230.9163 μg/g). This trend is consistent with the photocatalytic activity of the three samples.

## CONCLUSIONS

In summary, visible-light-driven plasmonic Bi/$ZnWO_4$ composite photocatalysts were successfully fabricated via a facile solvothermal process. Bi nanoparticles are well dispersed and deposited on the surface of $ZnWO_4$ microspheres, and the activity of the as-prepared composites was significantly improved for NO in air degradation as compared with pristine $ZnWO_4$. With the Bi to $ZnWO_4$ mass ratio of 0.5, the $B_{0.5}Z$ sample exhibits the highest activity among all the final products under visible light irradiation, which can be attributed to the synergistic effect of surface plasmon resonance (SPR) and the formation of the metal−semiconductor heterojunction interface. The construction of the Bi/$ZnWO_4$ plasmonic composite can remarkably improve the visible light absorption capability and enhance the separation/diffusion rate of the photogenerated charge carriers. The trapping experiments demonstrated that $\cdot O_2^-$ radical is the main active species for NO degradation, and ·OH is not involved in the photocatalytic degradation process. The coupling of semimetal Bi nanoparticles with semiconductor provides a new avenue to improve the photocatalytic performance, making the application of some UV light-responsive excellent photocatalytic materials possible.

## ASSOCIATED CONTENT

### Supporting Information

The Supporting Information is available free of charge on the ACS Publications website at DOI: 10.1021/acssuschemeng.6b01852.

Figures S1−S5 and Table S1 (PDF)

## AUTHOR INFORMATION

### Corresponding Author

*Phone: 86-29-6233 6261. E-mail: huangyu@ieecas.cn.

### Notes

The authors declare no competing financial interest.

## ACKNOWLEDGMENTS

This research was financially supported by the National Key Research and Development Program of China (2016YFA0203000), the National Science Foundation of China (41401567, 41573138), and the "Strategic Priority Research Program" of the Chinese Academy of Sciences (Grant No. XDB05000000) and was also partially supported by the research grant of Early Career Scheme (ECS 809813) from the Research Grant Council, Hong Kong SAR Government. Yu Huang is also supported by the "Hundred Talent Program" of the Chinese Academy of Sciences.

## REFERENCES

(1) Huang, R.-J.; Zhang, Y.; Bozzetti, C.; Ho, K. F.; Cao, J.-J.; Han, Y.; Daellenbach, K. R.; Slowik, J. G.; Platt, S. M.; Canonaco, F.; Zotter, P.; Wolf, R.; Pieber, S. M.; Bruns, E. A.; Crippa, M.; Ciarelli, G.; Piazzalunga, A.; Schwikowski, M.; Abbaszade, G.; Schnelle-Kreis, J.; Zimmermann, R.; An, Z.; Szidat, S.; Baltensperger, U.; El Haddad, I.; Prevot, A. S. High secondary aerosol contribution to particulate pollution during haze events in China. *Nature* **2014**, *514*, 218−222.

(2) Ball, J. C.; Hurley, M. D.; Straccia, A. M.; Gierczak, C. A. Thermal release of nitric oxide from ambient air and diesel particles. *Environ. Sci. Technol.* **1999**, *33*, 1175−1178.

(3) Hoffmann, M. R.; Martin, S. T.; Choi, W. Y.; Bahnemann, D. W. Environmental applications of semiconductor photocatalysis. *Chem. Rev.* **1995**, *95*, 69−96.

(4) Shang, L.; Bian, T.; Zhang, B. H.; Zhang, D. H.; Wu, L. Z.; Tung, C. H.; Yin, Y. D.; Zhang, T. R. Graphene-supported ultrafine metal nanoparticles encapsulated by mesoporous silica: robust catalysts for oxidation and reduction reactions. *Angew. Chem., Int. Ed.* **2014**, *53*, 250−254.

(5) Yu, J. G.; Yu, X. X. Hydrothermal synthesis and photocatalytic activity of zinc oxide hollow spheres. *Environ. Sci. Technol.* **2008**, *42*, 4902−4907.

(6) Li, H.; Zhou, Y.; Tu, W.; Ye, J.; Zou, Z. State-of-the-art progress in diverse heterostructured photocatalysts toward promoting photocatalytic performance. *Adv. Funct. Mater.* **2015**, *25*, 998−1013.

(7) Wang, H.; Zhang, L.; Chen, Z.; Hu, J.; Li, S.; Wang, Z.; Liu, J.; Wang, X. Semiconductor heterojunction photocatalysts: design, construction, and photocatalytic performances. *Chem. Soc. Rev.* **2014**, *43*, 5234−5244.

(8) Lin, J.; Lin, J.; Zhu, Y. F. Controlled synthesis of the $ZnWO_4$ nanostructure and effects on the photocatalytic performance. *Inorg. Chem.* **2007**, *46*, 8372−8378.

(9) Shi, R.; Wang, Y. J.; Li, D.; Xu, J.; Zhu, Y. F. Synthesis of $ZnWO_4$ nanorods with [100] orientation and enhanced photocatalytic properties. *Appl. Catal., B* **2010**, *100*, 173−178.

(10) Zhao, X.; Zhu, Y. F. Synergetic degradation of rhodamine B at a porous $ZnWO_4$ film electrode by combined electro-oxidation and photocatalysis. *Environ. Sci. Technol.* **2006**, *40*, 3367−3372.

(11) Chen, S. H.; Sun, S. X.; Sun, H. G.; Fan, W. L.; Zhao, X.; Sun, X. Experimental and theoretical studies on the enhanced photocatalytic activity of $ZnWO_4$ nanorods by fluorine doping. *J. Phys. Chem. C* **2010**, *114*, 7680−7688.

(12) Huang, Y.; Gao, Y.; Zhang, Q.; Cao, J.-j.; Huang, R.-j.; Ho, W.; Lee, S. C. Hierarchical porous $ZnWO_4$ microspheres synthesized by ultrasonic spray pyrolysis: characterization, mechanistic and photocatalytic $NO_x$ removal studies. *Appl. Catal., A* **2016**, *515*, 170−178.

(13) Dong, T. T.; Li, Z. H.; Ding, Z. X.; Wu, L.; Wang, X. X.; Fu, X. Z. Characterizations and properties of $Eu^{3+}$-doped $ZnWO_4$ prepared via a facile self-propagating combustion method. *Mater. Res. Bull.* **2008**, *43*, 1694−1701.

(14) Huang, G. L.; Zhang, S. C.; Xu, T. G.; Zhu, Y. F. Fluorination of $ZnWO_4$ photocatalyst and influence on the degradation mechanism for 4-chlorophenol. *Environ. Sci. Technol.* **2008**, *42*, 8516−8521.

(15) Li, P.; Zhao, X.; Jia, C.-j.; Sun, H.; Sun, L.; Cheng, X.; Liu, L.; Fan, W. $ZnWO_4$/BiOI heterostructures with highly efficient visible light photocatalytic activity: the case of interface lattice and energy level match. *J. Mater. Chem. A* **2013**, *1*, 3421−3429.

(16) Song, X. C.; Li, W. T.; Huang, W. Z.; Zhou, H.; Zheng, Y. F.; Yin, H. Y. A novel p-n heterojunction BiOBr/$ZnWO_4$: preparation and its improved visible light photocatalytic activity. *Mater. Chem. Phys.* **2015**, *160*, 251−256.

(17) Song, X. C.; Zheng, Y. F.; Yang, E.; Liu, G.; Zhang, Y.; Chen, H. F.; Zhang, Y. Y. Photocatalytic activities of Cd-doped $ZnWO_4$ nanorods prepared by a hydrothermal process. *J. Hazard. Mater.* **2010**, *179*, 1122−1127.



DOI: 10.1021/acssuschemeng.6b01852
ACS Sustainable Chem. Eng. XXXX, XXX, XXX−XXX

(18) Tian, N.; Huang, H.; Zhang, Y.; He, Y. Enhanced photocatalytic activities on $Bi_2O_2CO_3/ZnWO_4$ nanocomposites. *J. Mater. Res.* **2014**, *29*, 641−648.
(19) Wang, P.; Huang, B.; Dai, Y.; Whangbo, M. H. Plasmonic photocatalysts: harvesting visible light with noble metal nanoparticles. *Phys. Chem. Chem. Phys.* **2012**, *14*, 9813−9825.
(20) Zhang, Q.; Huang, Y.; Xu, L.; Cao, J. J.; Ho, W.; Lee, S. C. Visible-light-active plasmonic Ag-$SrTiO_3$ nanocomposites for the degradation of no in air with high selectivity. *ACS Appl. Mater. Interfaces* **2016**, *8*, 4165−4174.
(21) Caruana, A. J.; Cropper, M. D.; Stanley, S. A. Spontaneous growth of bismuth nanowires on a sputter-deposited thin bismuth film. *Surf. Coat. Technol.* **2015**, *271*, 8−12.
(22) O'Brien, B.; Plaza, M.; Zhu, L. Y.; Perez, L.; Chien, C. L.; Searson, P. C. Magnetotransport properties of electrodeposited bismuth films. *J. Phys. Chem. C* **2008**, *112*, 12018−12023.
(23) Yang, F. Y.; Liu, K.; Hong, K. M.; Reich, D. H.; Searson, P. C.; Chien, C. L. Large magnetoresistance of electrodeposited single-crystal bismuth thin films. *Science* **1999**, *284*, 1335−1337.
(24) Toudert, J.; Serna, R.; Jiménez de Castro, M. Exploring the optical potential of nano-bismuth: tunable surface plasmon resonances in the near ultraviolet-to-near infrared range. *J. Phys. Chem. C* **2012**, *116*, 20530−20539.
(25) Dong, F.; Xiong, T.; Sun, Y.; Zhao, Z.; Zhou, Y.; Feng, X.; Wu, Z. A semimetal bismuth element as a direct plasmonic photocatalyst. *Chem. Commun.* **2014**, *50*, 10386−10389.
(26) Weng, S.; Chen, B.; Xie, L.; Zheng, Z.; Liu, P. Facile in situ synthesis of a Bi/BiOCl nanocomposite with high photocatalytic activity. *J. Mater. Chem. A* **2013**, *1*, 3068−3075.
(27) Yu, Y.; Cao, C.; Liu, H.; Li, P.; Wei, F.; Jiang, Y.; Song, W. A Bi/BiOCl heterojunction photocatalyst with enhanced electron−hole separation and excellent visible light photodegrading activity. *J. Mater. Chem. A* **2014**, *2*, 1677−1681.
(28) Chang, C.; Zhu, L. Y.; Fu, Y.; Chu, X. L. Highly active Bi/BiOI composite synthesized by one-step reaction and its capacity to degrade bisphenol A under simulated solar light irradiation. *Chem. Eng. J.* **2013**, *233*, 305−314.
(29) Dong, F.; Li, Q. Y.; Sun, Y. J.; Ho, W. K. Noble metal-like behavior of plasmonic Bi particles as a cocatalyst deposited on (BiO)(2)CO3 microspheres for efficient visible light photocatalysis. *ACS Catal.* **2014**, *4*, 4341−4350.
(30) Xiong, T.; Dong, X.; Huang, H.; Cen, W.; Zhang, Y.; Dong, F. A single precursor mediated-synthesis of Bi semimetal deposited N-doped $(BiO)_2CO_3$ superstructures for highly promoted photocatalysis. *ACS Sustainable Chem. Eng.* **2016**, *4*, 2969−2979.
(31) Zhao, Z.; Zhang, W.; Sun, Y.; Yu, j.; Zhang, Y.; Wang, H.; Dong, F. Bi cocatalyst/$Bi_2MoO_6$ microspheres nanohybrid with SPR-promoted visible-light photocatalysis. *J. Phys. Chem. C* **2016**, *120*, 11889−11898.
(32) Dong, F.; Zhao, Z.; Sun, Y.; Zhang, Y.; Yan, S.; Wu, Z. An advanced semimetal-organic Bi spheres/g-$C_3N_4$ nanohybrid with spr-enhanced visible-light photocatalytic performance for no purification. *Environ. Sci. Technol.* **2015**, *49*, 12432−12440.
(33) Liu, X. W.; Cao, H. Q.; Yin, J. F. Generation and photocatalytic activities of Bi@$Bi_2O_3$ microspheres. *Nano Res.* **2011**, *4*, 470−482.
(34) Ma, J.; He, H.; Liu, F. Effect of Fe on the photocatalytic removal of $NO_x$ over visible light responsive Fe/$TiO_2$ catalysts. *Appl. Catal., B* **2015**, *179*, 21−28.
(35) Dong, F.; Lee, S. C.; Wu, Z. B.; Huang, Y.; Fu, M.; Ho, W. K.; Zou, S. C.; Wang, B. Rose-like monodisperse bismuth subcarbonate hierarchical hollow microspheres: One-pot template-free fabrication and excellent visible light photocatalytic activity and photochemical stability for NO removal in indoor air. *J. Hazard. Mater.* **2011**, *195*, 346−354.
(36) Li, R.; Chen, W.; Kobayashi, H.; Ma, C. Platinum-nanoparticle-loaded bismuth oxide: an efficient plasmonic photocatalyst active under visible light. *Green Chem.* **2010**, *12*, 212−215.
(37) Nyholm, R.; Berndtsson, A.; Martensson, N. Core level binding-energies for the elements hf to Bi (z = 72−83). *J. Phys. C: Solid State Phys.* **1980**, *13*, L1091−L1096.
(38) Wittstock, G.; Strubing, A.; Szargan, R.; Werner, G. Glucose oxidation at bismuth-modified platinum electrodes. *J. Electroanal. Chem.* **1998**, *444*, 61−73.
(39) Wang, Y. W.; Hong, B. H.; Kim, K. S. Size control of semimetal bismuth nanoparticles and the UV-visible and IR absorption spectra. *J. Phys. Chem. B* **2005**, *109*, 7067−7072.
(40) Wang, Z.; Jiang, C. L.; Huang, R.; Peng, H.; Tang, X. D. The investigation of optical and photocatalytic properties of bismuth nanospheres prepared by a facile thermolysis method. *J. Phys. Chem. C* **2014**, *118*, 1155−1160.
(41) Hou, W.; Cronin, S. B. A review of surface plasmon resonance-enhanced photocatalysis. *Adv. Funct. Mater.* **2013**, *23*, 1612−1619.
(42) Qu, L.; Luo, Z.; Tang, C. One step synthesis of Bi@$Bi_2O_3$@ carboxylate-rich carbon spheres with enhanced photocatalytic performance. *Mater. Res. Bull.* **2013**, *48*, 4601−4605.
(43) Ai, Z. H.; Ho, W. K.; Lee, S. C.; Zhang, L. Z. Efficient photocatalytic removal of NO in indoor air with hierarchical bismuth oxybromide nanoplate microspheres under visible light. *Environ. Sci. Technol.* **2009**, *43*, 4143−4150.


DOI: 10.1021/acssuschemeng.6b01852
*ACS Sustainable Chem. Eng.* XXXX, XXX, XXX−XXX